The Historic Rainfalls of Hurricanes Harvey and Florence: A Perspective from the Multi-Radar Multi-Sensor System

STEVEN M. MARTINAITIS,[a,b] STEPHEN B. COCKS,[a,b] ANDREW P. OSBORNE,[a,b] MICHEAL J. SIMPSON,[a,b] LIN TANG,[a,b] JIAN ZHANG,[b] AND KENNETH W. HOWARD[b]

[a] *Cooperative Institute for Mesoscale Meteorological Studies, University of Oklahoma, Norman, Oklahoma*
[b] *NOAA/OAR/National Severe Storms Laboratory, Norman, Oklahoma*

ABSTRACT: Hurricane Harvey in 2017 generated one of the most catastrophic rainfall events in United States history. Numerous gauge observations in Texas exceeded 1200 mm, and the record accumulations resulted in 65 direct fatalities from rainfall-induced flooding. This was followed by Hurricane Florence in 2018, where multiple regions in North Carolina received over 750 mm of rainfall. The Multi-Radar Multi-Sensor (MRMS) system provides the unique perspective of applying fully automated seamless radar mosaics and locally gauge-corrected products for these two historical tropical cyclone rainfall events. This study investigates the performance of various MRMS quantitative precipitation estimation (QPE) products as it pertains to rare extreme tropical cyclone rainfall events. Various biases were identified in the radar-only approaches, which were mitigated in a new dual-polarimetric synthetic radar QPE approach. A local gauge correction of radar-derived QPE provided statistical improvements over the radar-only products but introduced consistent underestimation biases attributed to undercatch from tropical cyclone winds. This study then introduces a conceptual methodology to bulk correct for gauge wind undercatch across the numerous gauge networks ingested by the MRMS system. Adjusting the hourly gauge observations for wind undercatch resulted in increased storm-total accumulations for both tropical cyclones that better matched independent gauge observations, yet its application across large network collections highlighted the challenges of applying a singular wind undercatch correction scheme for significant wind events (e.g., tropical cyclones) while recognizing the need for increased metadata on gauge characteristics.

KEYWORDS: Precipitation; Rainfall; Tropical cyclones; Radars/Radar observations; Wind effects

1. Introduction

Two historical tropical cyclone rain events occurred over the contiguous United States (CONUS) within a 13-month period. Hurricane Harvey in August 2017 resulted in the largest tropical cyclone precipitation accumulation event in the history of the United States, which produced catastrophic flooding across southeastern Texas (Blake and Zelinsky 2018). Eighteen rain gauge observations in southeast Texas accumulated more than 1220 mm (48.0 in.) of rain along with a record 1538.7 mm (60.58 in.) storm total rainfall near Nederland, Texas, from 25 August to 4 September 2017. Hurricane Florence produced record rainfall and rainfall-induced flooding across the Carolinas in September 2018 (Stewart and Berg 2019). Fifteen rain gauge observations accumulated more than 610 mm (24.0 in.) of rain across North Carolina, including a maximum of 912.6 mm (35.93 in.) northwest of Elizabethtown, North Carolina, from 13 to 18 September 2018.

The historic rainfall from Harvey and Florence combined for 90 direct fatalities in the CONUS (Blake and Zelinsky 2018; Stewart and Berg 2019). A total of 82 direct fatalities (91.1%) were attributed to freshwater flooding, including all but 3 of the 68 direct fatalities (95.6%) from Hurricane Harvey. Of the 22 direct fatalities from Hurricane Florence, 17 (77.3%) were attributed to freshwater flooding. Damage sustained during Hurricane Harvey was estimated at $125 billion, making it one of the costliest tropical cyclones to impact the United States (Blake and Zelinsky 2018). The excessive rainfall totals within populated regions, especially the Houston, Texas, metropolitan area, resulted in the flooding of over 300 000 structures and approximately 500 000 vehicles. Hurricane Florence generated an estimated $24 billion in damage (Stewart and Berg 2019). The majority of losses came from freshwater flooding, including damage to numerous commercial and residential structures along with losses to agriculture and livestock.

In situ and remote sensing observations recorded various meteorological aspects of Hurricanes Harvey and Florence during their life cycles, including estimated precipitation accumulations over land. One platform reliant upon multiple observational networks is the Multi-Radar Multi-Sensor (MRMS) system (Zhang et al. 2016). The MRMS system is both an operational and research platform designed to incorporate various observational datasets and numerical weather prediction (NWP) for the generation of high spatiotemporal resolution products, including a suite of quantitative precipitation estimations (QPEs). The MRMS system contains a series of algorithms improving the quality and accuracy of QPEs that include the removal of nonmeteorological echoes (Tang et al. 2014), the mitigation of bright-banding in the melting layer (Zhang and Qi 2010; Qi et al. 2013), seamless mosaicking of 3D radar reflectivities (Qi and Zhang 2017), accounting for the evaporation of hydrometeors (Martinaitis et al. 2018), and an advanced quality control (QC) of automated hourly gauge observations (Qi et al. 2016) for local gauge correction of radar-derived QPE (Zhang et al. 2016). Research studies and

---

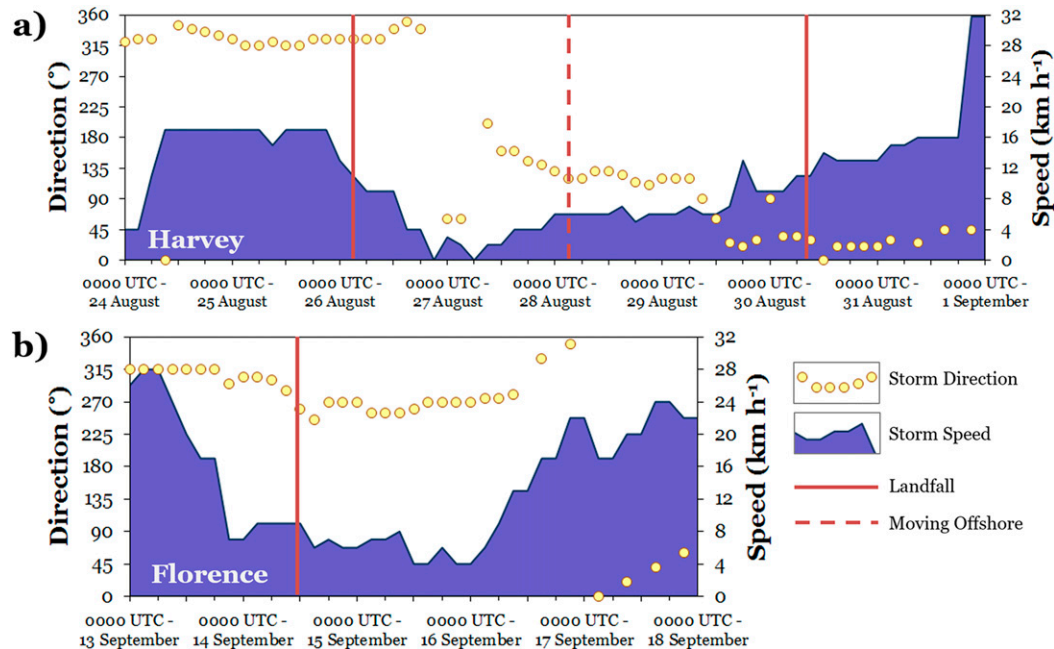*Corresponding author*: Steven M. Martinaitis, steven.martinaitis@noaa.gov

FIG. 1. Time series of the storm direction (°; yellow circles) and storm speed (km h^{-1}; blue color fill) for (a) Hurricane Harvey during the period 0000 UTC 24 Aug–0000 UTC 1 Sep 2017 and (b) Hurricane Florence during the period 0000 UTC 13 Sep–0000 UTC 18 Sep 2018. The solid red line represents the time of landfall, and the dashed red line represents the time of moving offshore. Storm motion data and the times of landfall and moving offshore were provided by the National Hurricane Center (NHC; https://www.nhc.noaa.gov).

precipitation estimation intercomparisons have demonstrated the effectiveness of the aforementioned algorithms on the performance of MRMS QPEs (e.g., Cocks et al. 2016, 2017).

It is important to understand the current skill and challenges of generating accurate rainfall accumulations during landfalling tropical cyclones for critical decision support services and hydrologic modeling, especially for tropical cyclones that produce extreme rainfall totals and catastrophic rainfall-induced flooding. This study presents an evaluation of the MRMS hydrometeorological products for two extreme tropical cyclone precipitation events. Performance tendencies of two different radar-derived MRMS QPEs were examined along with a locally gauge-corrected radar QPE. This study then addresses the challenges of measuring accumulations of wind-driven rain via a conceptual bulk wind correction scheme for hourly gauge observations. Broadscale implementation of a wind correction scheme highlights the need for further research on correcting for wind-driven undercatch in tropical cyclone winds while demonstrating the challenges of implementing a large-scale wind correction scheme across vast gauge network collections.

2. Meteorological overviews of Harvey and Florence

Harvey formed as a tropical depression around 0600 UTC 17 August 2017 approximately 815 km east of Barbados. It was classified as a tropical storm at 1800 UTC 17 August but degenerated into a tropical wave 48 h later in the Caribbean Sea. Regeneration began on 23 August 2017 followed by a rapid

intensification up to the initial CONUS landfall on San Jose Island, Texas, at 0300 UTC 26 August with maximum sustained winds of 115 kt (59.2 m s^{-1}) and an estimated minimum central pressure of 937 hPa. Harvey decelerated over Texas following landfall and looped back to the east-southeast where it reemerged over the Gulf of Mexico at 0300 UTC 28 August. A forward speed of <4.9 kt (9.0 km h^{-1}) was recorded for 81 consecutive hours from 0600 UTC 26 August to 1500 UTC 29 August 2017, including two periods of stationary motion (Fig. 1a). Final landfall occurred in southwestern Louisiana at 0800 UTC 30 August as Harvey accelerated to the northnortheast. For a complete discussion on Hurricane Harvey, see Blake and Zelinsky (2018).

Florence was classified as a tropical depression around 1800 UTC 31 August 2018 and classified as a tropical storm 12 h later approximately 200 km west-southwest of the Cabo Verde Islands. Florence gradually strengthened and reached hurricane status on 4 September, which was followed by a rapid intensification to category 4 by 1800 UTC 5 September. Fluctuations in strength occurred over several days until its landfall near Wrightsville Beach, North Carolina, at 1115 UTC 14 September with maximum sustained winds of 80 kt (41.2 m s^{-1}) and an estimated central pressure of 956 hPa. A weakening ridge and lack of steering currents kept the center of Florence over North and South Carolina for 3 days. Florence had 57 consecutive hours of a forward motion < 4.9 kt (9.0 km h^{-1}) from 2100 UTC 13 September to 0600 UTC 16 September (Fig. 1b). For a complete discussion on Hurricane Florence, see Stewart and Berg (2019).
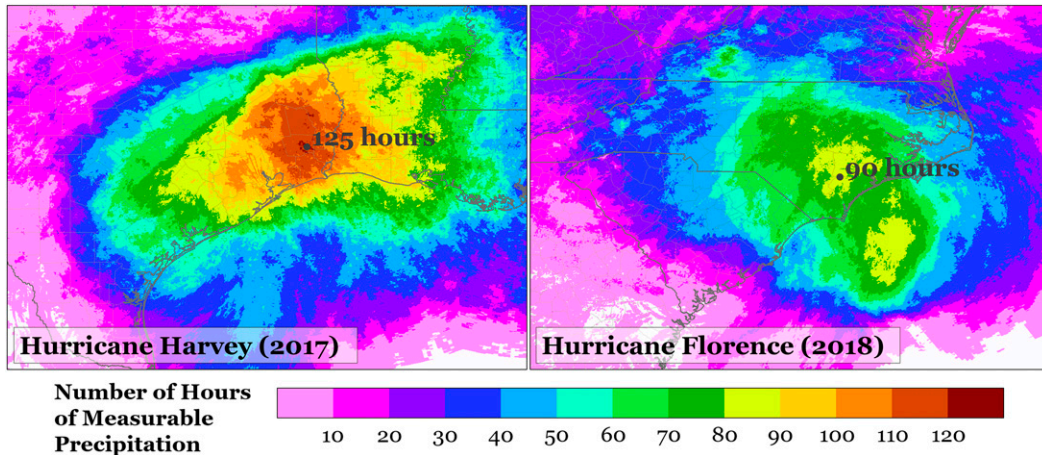
FIG. 2. Number of hours that recorded top-of-the-hour rainfall accumulations ≥ 0.254 mm (0.01 in.) for (a) Hurricane Harvey during the period from 0000 UTC 24 Aug to 0000 UTC 1 Sep 2017 and (b) Hurricane Florence during the period from 0000 UTC 13 Sep to 0000 UTC 17 Sep 2018. The location denoted in each figure identifies the maximum number of hours that recorded top-of-the-hour rainfall accumulations ≥ 0.254 mm.

The slow forward motion of both tropical cyclones exacerbated the associated freshwater flooding by greatly enhancing rainfall durations. Counts of top-of-the-hour MRMS hourly precipitation accumulations showed expansive regions recording at least 0.254 mm (0.01 in.) rainfall for ≥40 h during both events (Fig. 2). Areas recording measurable precipitation for at least 40 h during Hurricane Harvey covered 257 785 km^2 over land (Table 1), which is equivalent to the size of Oregon. Locations receiving at least 80 h of hourly rainfall accumulations > 0.254 mm covered approximately 102 685 km^2, an area equivalent to the size of Kentucky. An estimated 35 585 km^2 of area over land recorded at least 100 h of hourly rainfall with a maximum of 125 h in southern Hardin County, Texas. The area over land that recorded rainfall for at least 40 h of measurable hourly rainfall accumulations during Hurricane Florence was 147 487 km^2, which was just larger than the state of Iowa (Table 1). An estimated 45.1% of this area (or 66 946 km^2) had at least 60 h of recorded hourly rainfall. A maximum of 90 h was identified in southwest Duplin County, North Carolina.

3. Products and methodology

a. MRMS QPE products

1) RADAR-ONLY SCHEMES

Two MRMS radar-only QPEs were generated for both tropical cyclone events: a reflectivity-only QPE (Q_{RAD}) and a dual-polarization synthetic QPE (Q_{DP}). The QPE Q_{RAD} relied on reflectivity properties from the seamless hybrid scan reflectivity product and NWP environmental data to classify a surface precipitation type (SPT) and utilize different empirical rate–reflectivity $R(Z)$ relationships at each MRMS grid cell. A full description of the Q_{RAD} scheme and its inputs can be found in Zhang et al. (2016). The QPE Q_{DP} exploited different radar and dual-polarization variables compared to the position of the radar beam relative to the melting layer. Precipitation rates based on specific attenuation $R(A)$ were used in pure rainfall

below the melting layer melting layer, specific differential phase in convective cores where hail was likely, and $R(Z)$ within and above the melting layer. A full description of the Q_{DP} scheme can be found in Wang et al. (2019) and Zhang et al. (2020). Final Q_{DP} rates were modified to account for evaporative impacts between the radar beam and the surface (Martinaitis et al. 2018).

2) LOCALLY GAUGE-CORRECTED RADAR QPE

A locally gauge-corrected radar QPE (Q_{LGC}) was generated from the hourly accumulations of the Q_{DP} product. The MRMS system utilized hourly automated gauge observations from the Hydrometeorological Automated Data System (HADS; Kim et al. 2009) and the Meteorological Assimilation Data Ingest System (MADIS; Helms et al. 2009) networks that passed the gauge QC algorithm described by Qi et al. (2016) and modified by Martinaitis et al. (2018). Passing gauge observations were compared to collocated gridded 1-h Q_{DP} values, and the local biases were interpolated through an inverse distance weighting (IDW) scheme with varying interpolation radii based on a cross validation methodology. A description of the generation of Q_{LGC} can be found in Zhang et al. (2016).

3) WIND-CORRECTED QPE

The local gauge correction methodology for Q_{LGC} is reliant upon the accuracy of the gauge observations; yet, various

TABLE 1. The area over land (km^2) based on the number of hours that recorded precipitation ≥ 0.254 mm (0.01 in.) from top-of-the-hour analysis of MRMS precipitation accumulations.

No. of hours	Harvey (2017)	Florence (2018)
≥40	257 785	147 487
≥60	177 801	66 946
≥80	102 685	8380
≥100	35 585	0
≥120	417	0

TABLE 2. List of the previous studies and equations that were used to calculate the prototype wind correction algorithm for testing in the MRMS system. Included are the studies referenced, the gauge types, shielding configurations, the wind undercatch ratio equations, and accumulation periods focused on in each study. The wind undercatch ratio equations are all based on the wind speed u with some equations also influenced by the rain rate R.

Study	Gauge type	Shield	Ratio equation	Accumulation
Allerup and Madsen (1980)	Hellman 8 in.	None	$\exp\{[-0.0010 \times \ln(R)] - [0.0082 \times u \times \ln(R)] + (0.0420 \times u) + 0.0100\}$	Instantaneous
Førland et al. (1996)	Hellman 8 in.	Alter type	$\exp\{[-0.001\,01 \times \ln(R)] - [0.012\,177 \times u \times \ln(R)] + (0.034\,331 \times u) + 0.007\,697 - 0.05\}$	Instantaneous
Førland and Hanssen-Bauer (2000)	Hellman 8 in.	None	$\exp\{[-0.001\,01 \times \ln(R)] - [0.012\,177 \times u \times \ln(R)] + (0.034\,331 \times u) + 0.007\,697\}$	Instantaneous
Yang et al. (1998)	NWS 8 in.	None	$\exp[4.605 - (0.062 \times u^{0.58})]$	Daily
Yang et al. (1998)	NWS 8 in.	Alter type	$\exp[4.606 - (0.041 \times u^{0.69})]$	Daily

studies have identified systematic underestimation biases attributed to wind-induced undercatch and introduced mathematical solutions to correct observational values (e.g., Allerup and Madsen 1980; Førland et al. 1996; Yang et al. 1998). These calculations utilized either instantaneous wind speed values or daily wind speed averages of ≤15.0 m s^{-1}, which are below the minimum wind classifications for a tropical storm (17.5 m s^{-1}) and hurricane (32.9 m s^{-1}); moreover, the correction equations were derived for either instantaneous precipitation rates or daily accumulations.

This study introduces the concept of implementing a single bulk wind correction scheme across multiple networks within the MRMS framework. The proposed design was similar to Medlin et al. (2007) by blending recent research findings into a single equation to adjust hourly gauge accumulations. Five equations from four studies (Allerup and Madsen 1980; Førland et al. 1996; Yang et al. 1998; Førland and Hanssen-Bauer 2000) were considered in the conceptual wind correction algorithm (Table 2). These studies utilized gauges with a 20.32-cm (8 in.) diameter opening, and the equations were derived for either shielded or unshielded gauges. Previous studies have shown that including an Alter-type windshield reduced wind undercatch by ≤3% (Duchon and Essenberg 2001; Yang et al. 1998); thus, the small differences between shielded and unshielded gauges allowed for the combining of all equations in Table 2 for a singular bulk-use equation. Three equations included the rainfall rate R within the calculations. A fixed value of $R = 50$ mm h^{-1} was utilized in the conceptual design. Variations of R were shown to have minimal impact on the gauge correction ratio. The correction ratio differed by 0.2%–1.2% when varying R from 50 to 25 mm h^{-1}.

Gauge correction ratios were calculated for each equation in Table 2 for wind speeds of 1–20 m s^{-1} (Fig. 3). An exponential function was fitted to the data to generate the conceptual wind correction multiplier G_C for hourly gauge rainfall accumulations,

$$G_C = 1.0184 e^{0.0276 U(h)}, \qquad (1)$$

where $U(h)$ is the wind speed at the gauge height AGL. The wind speed $U(h)$ was interpolated from the 10 m AGL wind generated by the High-Resolution Rapid Refresh (HRRR;

Benjamin et al. 2016) model via the following logarithmic equation from Yang et al. (1998):

$$U(h) = \frac{[\ln(h/z_0)]}{[\ln(H/z_0)]} U(H), \qquad (2)$$

where $U(H)$ is the HRRR model wind speed at a height $H = 10$ m, h is the height of the gauge AGL and was set at 1.00 m based on the standard NWS gauge height reference (Yang et al. 1998), and z_0 is the roughness parameter defined as 0.03 m for short grass in warm season months.

Equation (1) was multiplied to hourly gauge totals when the interpolated wind speed from Eq. (2) was ≥1.0 m s^{-1}. The extrapolation of Eq. (1) out to 40 m s^{-1} had some similarities to the estimated errors by Medlin et al. (2007). Correction ratios of 1.34 and 1.54 were generated at $u = 10$ and 15 m s^{-1}, respectively. This was less than the ratios of 1.60 and 1.80 from Medlin et al. (2007) at equivalent wind magnitudes. A ratio of 2.03 via Eq. (1) was calculated at $u = 25$ m s^{-1}, which complimented the correction ratio of 2.00 by Medlin et al. (2007) at that wind speed. Gauges modified via Eq. (1) were then used in the locally gauge-correction algorithm to generate a new wind-corrected Q_{LGC} product (denoted as Q_{WC}).

b. QPE analysis methodology

MRMS QPE analyses for Hurricane Harvey were conducted over an 8-day period from 0000 UTC 24 August to 0000 UTC 1 September 2017 for a domain bounded by the northwest corner 33.0°N, 100.0°W and the southeast corner 26.0°N, 90.0°W. Hurricane Florence was evaluated over a 5-day period from 0000 UTC 13 September to 0000 UTC 18 September 2018 for a domain bounded by the northwest corner 38.0°N, 84.0°W and the southeast corner 31.0°N, 74.0°W. Emphasis on daily accumulations and comparisons were conducted for 24-h periods ending 1200 UTC 26–28 August for Harvey and 1100 UTC 15–17 September for Florence.

All regional Weather Surveillance Radar-1988 Doppler (WSR-88D) radars were available for Harvey; however, three critical WSR-88D radars became unavailable during Florence. The Wilmington, North Carolina, WSR-88D radar (KLTX) experienced outages from 2138 UTC 14 September to 0238 UTC 15 September, 1338–1900 UTC 15 September, and 2110–2200 UTC 15 September. Data quality issues were also
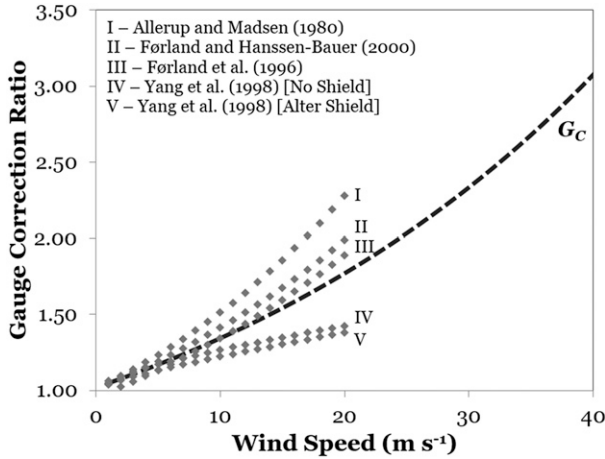
FIG. 3. Graph of the gauge wind correction ratio G_C (black dashed line) as defined by the equations of the five studies listed in Table 2 (gray dotted lines). The five equations from the previous studies are extrapolated out to 20 m s^{-1}. The prototype G_C ratio is interpolated out to 40 m s^{-1}.

prevalent prior to the second and third outages. The Morehead City, North Carolina, WSR-88D radar (KMHX) failed at 1946 UTC 15 September and was unavailable through 0102 UTC 20 September. The Columbia, South Carolina, WSR-88D radar (KCAE) was unavailable from 0520 to 1346 UTC 16 September. These multiple outages were reflected in the MRMS radar quality index (Zhang et al. 2012) and seamless hybrid scan reflectivity height (Zhang et al. 2016) products (Fig. 4).

Hourly MRMS QPE products were accumulated and statistically compared to Community Collaborative Rain, Hail and Snow (CoCoRaHS) daily gauge observations (Cifelli et al. 2005). Comparative accumulations included 24-h and storm-total summations. The CoCoRaHS rain gauge is a clear plastic cylinder with a 10.16-cm diameter that can measure up to 279.4 mm. Observations are taken by volunteers generally at 0700 local time ± 2 h. Verifying CoCoRaHS observations were not adjusted for wind undercatch errors. Nešpor and Sevruk (1999) showed through numerical simulations that the integral wind-induced error was less significant for gauges with a smaller orifice diameter; moreover, there were a lack of studies relating to wind undercatch correction at the CoCoRaHS gauge orifice diameter scale that do not allow for a proper correction of CoCoRaHS gauge observations. Gauge measurement limiting factors based on subjective biases of human observers must be considered (Daly et al. 2007). Additional recording challenges also exist with tropical cyclones. The potential inability to safely conduct measurements during a tropical cyclone could occur. Potential errors and approximations with extreme daily precipitation totals exceeding the maximum cylinder measurement of 279.4 mm were likely if unmeasured overflow occurred during the 24-h reporting time.

The Q_{WC} product was also compared against the NWS Stage IV QPE, a combination of WSR-88D radar QPE and gauge observations generated by NWS river forecast centers (Lin and Mitchell 2005). Statistical analyses of Stage IV QPEs versus CoCoRaHS were not conducted, since CoCoRaHS gauges were not independent to Stage IV QPE. Gridded differences between Stage IV and the MRMS Q_{WC} products were generated for both Harvey and Florence. NWS Stage IV 24-h QPE
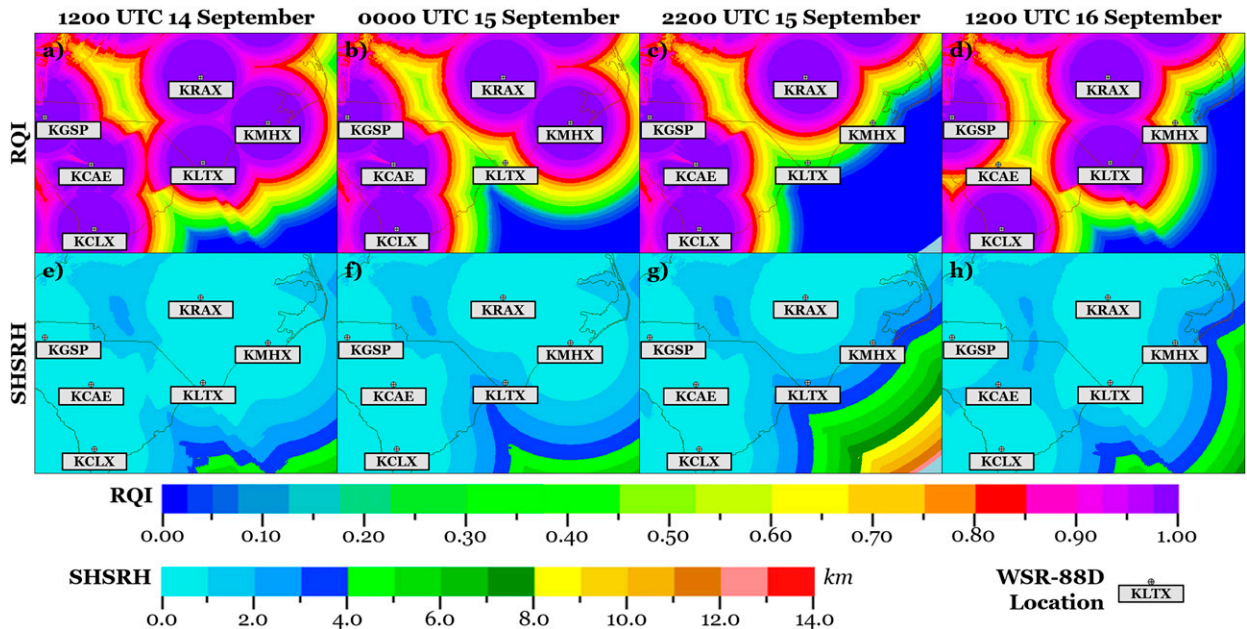

FIG. 4. Depiction of WSR-88D radar coverage and the impacts of various radar outages during Florence from the perspective of (top) the MRMS radar quality index (RQI) and (bottom) seamless hybrid scan reflectivity height (SHSRH) products for the periods (a),(e) 1200 UTC 14 Sep; (b),(f) 0000 UTC 15 Sep; (c),(g) 2200 UTC 15 Sep; and (d)–(h) 1200 UTC 16 Sep 2018. RQI values of 1.00 represent unobstructed radar coverage below the melting layer with decreasing RQI values depicting a reduction in adequacy of radar coverage.
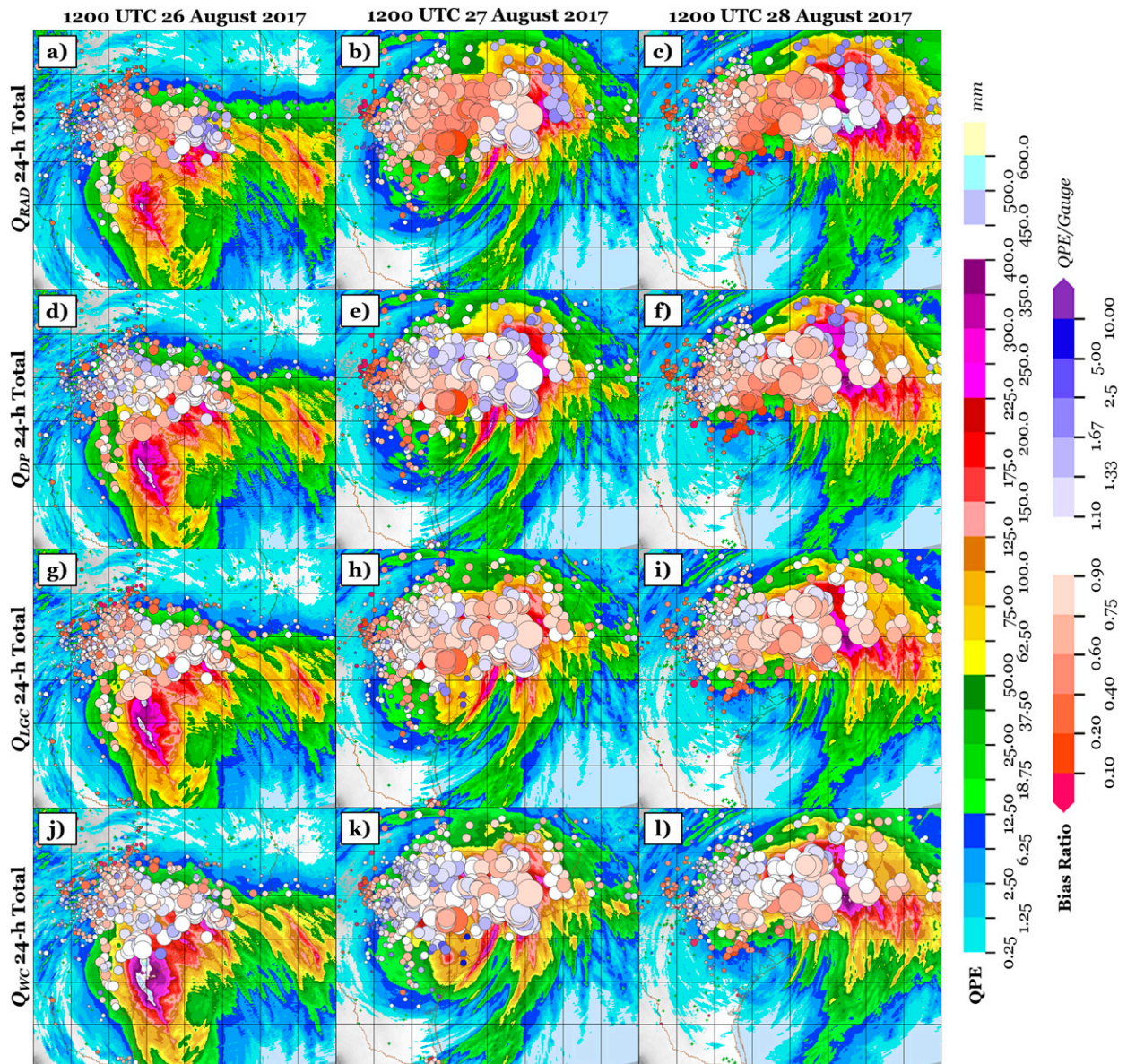
FIG. 5. Bubble plots of CoCoRaHS daily gauge observations with 24-h accumulations (mm) of (a)–(c) Q_{RAD}, (d)–(f) Q_{DP}, (g)–(i) Q_{LGC}, and (j)–(l) Q_{WC} during Hurricane Harvey for the 24-h periods ending (left) 1200 UTC 26 Aug, (center) 1200 UTC 27 Aug, and (right) 1200 UTC 28 Aug 2017. Bubble plots are represented based on precipitation totals (size) and the bias ratio (color fill) based on the MRMS gridded QPE product divided by the CoCoRaHS observation. Warm colors denote an underestimation bias by the MRMS QPE product. Cool colors denote an overestimation bias by the MRMS QPE product.

are generated daily at 1200 UTC; thus, gridded comparisons were conducted from 1200 UTC 24 August to 1200 UTC 31 August 2017 for Harvey and 1200 UTC 13 September to 1200 UTC 17 September 2018 for Florence.

4. MRMS product results

a. Radar-based daily accumulations

Distinct precipitation biases were depicted in the two MRMS radar-only QPEs when compared to CoCoRaHS gauge observations. Bubble plot analysis of 24-h Q_{RAD} accumulations were

characterized by underestimations in areas predominantly experiencing stratiform precipitation types, especially related to the central dense overcast region, for both Hurricane Harvey (Figs. 5a–c) and Florence (Figs. 6a–c). Regions experiencing precipitation underestimations were also influenced by the WSR-88D radars overshooting critical warm rain processes less than 1 km above ground level. Various radar outages during Florence further exacerbated the underestimation bias coverage and magnitude. A contrasting overestimation bias was depicted in areas experiencing prolonged convective precipitation. This was notable around the Houston, Texas region for the period
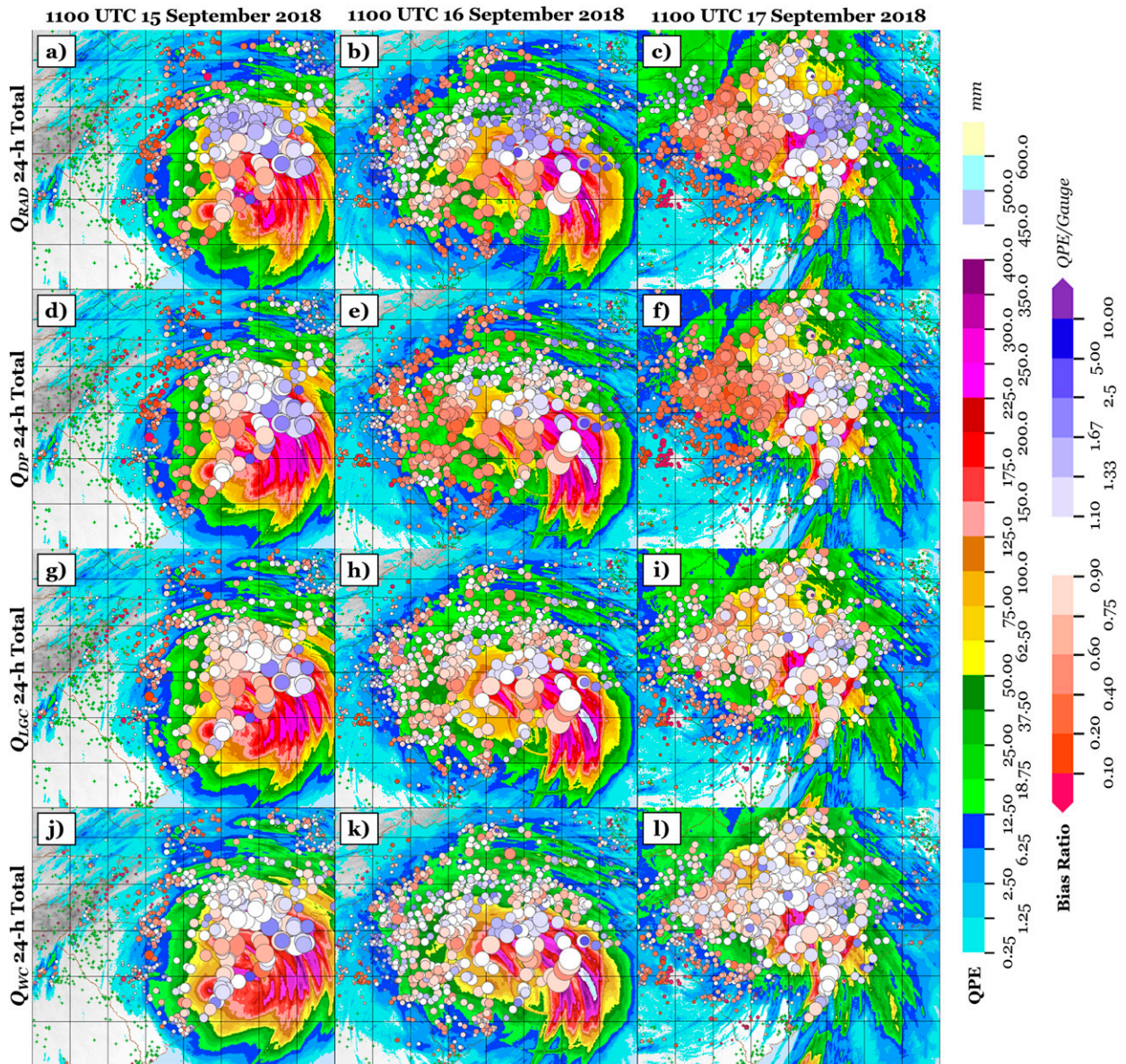
FIG. 6. As in Fig. 5, but during Hurricane Florence for the 24-h periods ending (left) 1100 UTC 15 Sep, (center) 1100 UTC 16 Sep, and (right) 1100 UTC 17 Sep 2018.

ending 1200 UTC 26 August (Fig. 5a) and far eastern Texas during 27–28 August 2017 (Figs. 5b,c) during Hurricane Harvey as well as the areas influenced by the convective bands in southeastern North Carolina (Figs. 6a–c) during Hurricane Florence.

The MRMS Q_{DP} accumulations exhibited similar bias tendencies with general improvements in both the stratiform underestimation biases and the convective overestimation biases for both storms (Figs. 5d–f and 6d–f), yet there were a few instances when Q_{DP} performance remained similar or degraded compared to Q_{RAD}. Greater convective overestimation biases existed near the Houston area during Harvey on 27 August 2017 (Fig. 5e), and slightly greater underestimation

biases were noted in some stratiform accumulation totals, notably around the southern periphery of Harvey on 28 August 2017 (Fig. 5f). Similar trends in Q_{DP} performance were seen in Hurricane Florence. Greater overestimation biases were observed in convective features over southern North Carolina on 15 September (Fig. 6d) and greater underestimation biases in the western quadrant of Florence on 17 September (Fig. 6f).

Differences in rate calculations were highlighted between the two radar-based methodologies for both Harvey and Florence. The SPT approach using $R(Z)$ yielded tropical-based classifications for most grid cells (Figs. 7a,b). Tropical classifications were applied when reflectivity values were ≥15 dBZ, and warm stratiform was applied elsewhere in stratiform
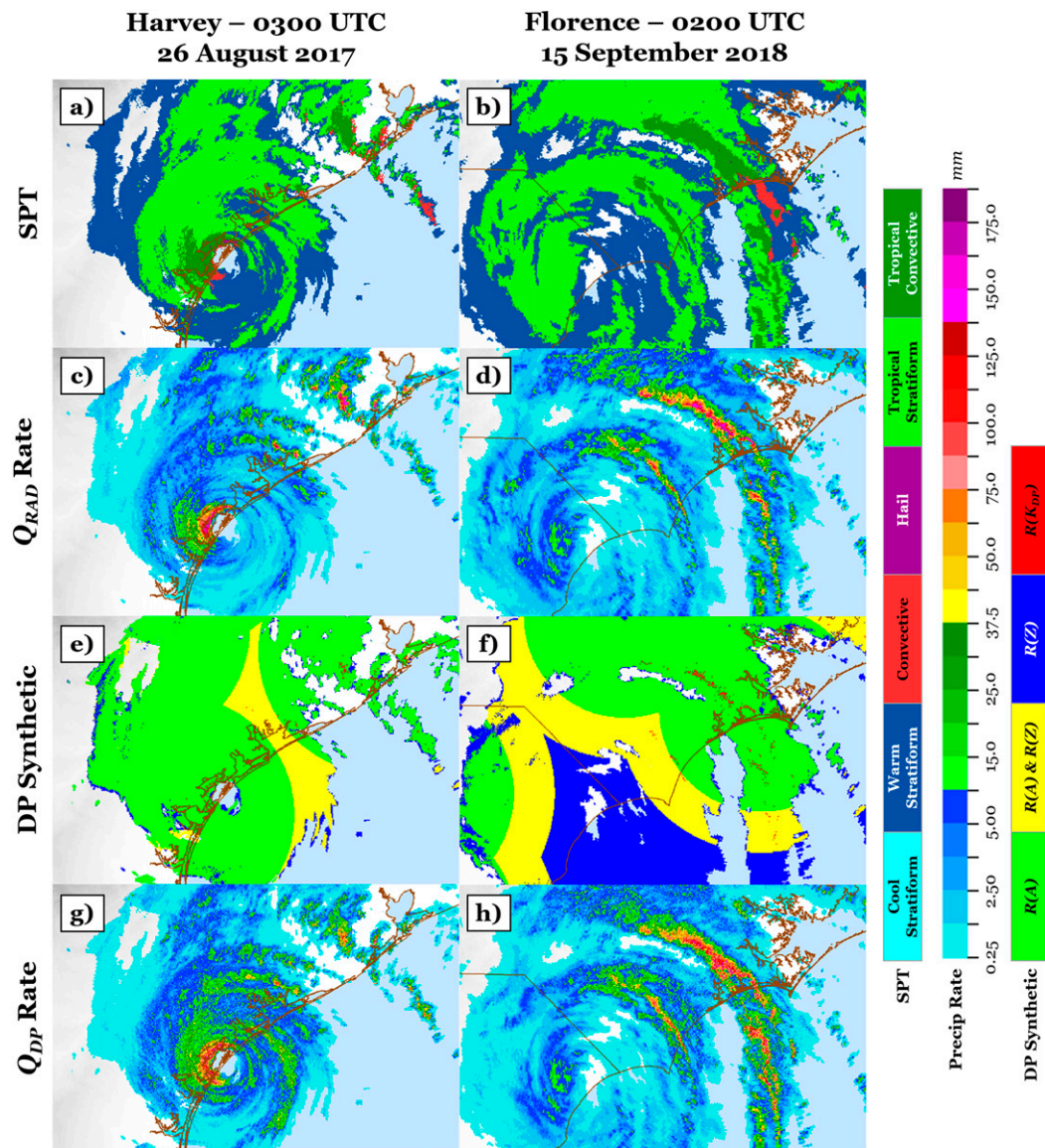
Harvey – 0300 UTC 26 August 2017

Florence – 0200 UTC 15 September 2018

FIG. 7. Analysis of the (a),(b) MRMS surface precipitation type (SPT) classification; (c),(d) Q_{RAD} instantaneous precipitation rate based on SPT (mm); (e),(f) dual-polarization (DP) synthetic flag; and (g),(h) Q_{DP} instantaneous precipitation rate based on DP synthetic flag (mm) (left) during Hurricane Harvey for 0300 UTC 26 Aug and (right) during Hurricane Florence for 0200 UTC 15 Sep 2018.

precipitation types. Convective and tropical convective classifications were utilized in the eyewall and banding features. The few $R(Z)$ relationships applied to MRMS Q_{RAD} were likely not representative of the drop size distributions that exist in tropical cyclones. The dual-polarization synthetic approach relied on the location of reflectivity data with respect to the melting layer. The $R(A)$ calculations were applied below the melting layer while an $R(Z)$ transition occurred when within and above the melting layer (Figs. 7e,f). The employment of $R(A)$ demonstrated the ability to improve precipitation estimations by being insensitive to drop size distributions associated with stratiform or convective precipitation regardless of whether it occurs within a tropical

or continental rain regime (e.g., Ryzhkov et al. 2014; Wang et al. 2019; Cocks et al. 2019).

The precipitation rate differences characterize the influence of moving from strictly $R(Z)$ approach to a dual-polarization methodology (Fig. 7). The MRMS Q_{DP} scheme tempered some of the convective-based rain rates overestimations when compared to Q_{RAD}, as evident in the eyewall convection and the cell southwest of Houston for Harvey (Figs. 7c,g). Improvements in underestimation biases with stratiform precipitations were shown in the rain rate increases in Q_{DP}. The central dense overcast region for Harvey at 0300 UTC 26 August 2017 had instantaneous Q_{RAD} precipitation rates $\leq$ 10.16 mm h^{-1} (0.40 in. h^{-1};

TABLE 3. Statistical analysis of the MRMS Q_{RAD}, Q_{DP}, Q_{LGC}, and Q_{WC} products for the 24-h periods ending 1200 UTC for 26–28 Aug 2017 along with a 3-day average for each MRMS QPE product. Included are the mean bias ratio (MRMS QPE product divided by the CoCoRaHS gauge values), mean absolute error (MAE), and correlation coefficient (CC).

Product	Date	Mean bias ratio	MAE (mm)	CC
Q_{RAD}	26 Aug	0.889	10.719	0.878
	27 Aug	0.818	30.099	0.884
	28 Aug	0.843	19.152	0.893
	3-day average	0.850	19.990	0.885
Q_{DP}	26 Aug	0.957	7.264	0.946
	27 Aug	0.997	23.368	0.931
	28 Aug	0.835	16.713	0.930
	3-day average	0.930	15.782	0.936
Q_{LGC}	26 Aug	0.852	7.010	0.963
	27 Aug	0.905	20.523	0.942
	28 Aug	0.851	13.335	0.960
	3-day average	0.869	13.623	0.955
Q_{WC}	26 Aug	0.977	6.426	0.956
	27 Aug	1.033	19.279	0.944
	28 Aug	0.949	11.684	0.962
	3-day average	0.986	12.463	0.954

TABLE 4. As in Table 3, but for Hurricane Florence (2018) for the 24-h periods ending 1100 UTC for 15–17 Sep 2018.

Product	Date	Mean bias ratio	MAE (mm)	CC
Q_{RAD}	15 Sep	1.130	9.652	0.929
	16 Sep	0.987	10.058	0.888
	17 Sep	0.883	15.291	0.848
	3-day average	1.000	11.667	0.888
Q_{DP}	15 Sep	1.011	8.077	0.926
	16 Sep	0.760	10.490	0.890
	17 Sep	0.718	14.554	0.871
	3-day average	0.830	11.040	0.896
Q_{LGC}	15 Sep	0.927	6.172	0.944
	16 Sep	0.870	6.985	0.938
	17 Sep	0.882	8.687	0.942
	3-day average	0.893	7.281	0.941
Q_{WC}	15 Sep	1.024	5.918	0.947
	16 Sep	0.973	6.502	0.940
	17 Sep	0.954	8.103	0.944
	3-day average	0.984	6.841	0.944

Fig. 7c) while >20.32 mm h^{-1} characterized a greater percentage of the same region using Q_{DP} (Fig. 7g). These performance changes coincided with the findings from Zhang et al. (2020) when comparing Q_{RAD} and Q_{DP} accumulations. Similar results were found in the northern semicircle of Florence; however, no improvement was shown in the southern semicircle (Figs. 7d,h). The lack of improvements between Q_{RAD} and Q_{DP} during Florence can be attributed to reduced radar coverage from the various outages (e.g., Fig. 7f), which resulted in the dual-polarization $R(Z)$ methodology being applied and, thus, Q_{DP} was near equivalent to Q_{RAD}.

The noted variations between the two MRMS radar-based schemes were reflected in the statistical analyses. Improved 3-day averages from the Q_{RAD} accumulations to the Q_{DP} accumulations were shown for all statistical metrics during Hurricane Harvey (Table 3). The average underestimation mean bias ratio was reduced by 53%, and the average mean absolute error (MAE) decreased by 21% from 19.99 to 15.78 mm. The correlation coefficient improved by 0.051 from an average of 0.885 with Q_{RAD} to 0.936 with Q_{DP}. This was reflected in each daily evaluation with the exception of a slight degradation in the mean bias ratio from Q_{RAD} to Q_{DP} for the 24-h period ending 1200 UTC 28 August 2017.

Average statistical measures lacked improvement between Q_{RAD} and Q_{DP} for Florence across its highlighted 3-day period (Table 4). The average MAE decreased by approximately 5% with Q_{DP}, and the average correlation coefficient value were similar; moreover, the overall mean bias ratio degraded with the Q_{DP} accumulations. The average mean bias ratio for Q_{RAD} was 1.00 across the 3-day period, yet the authors argue that this perception of an ideal bias ratio was generated from the balance between the significant overestimation and underestimation features for

each day. The decrease in the average Q_{DP} mean bias ratio to 0.83 was attributed to the various WSR-88D radar outages, which limited the sampling of critical low-altitude dual-polarization characteristics that would better represent efficient tropical rainfall (i.e., not mitigating the underestimation biases in the stratiform precipitation types), in combination with the reduction of overestimation biases within the convective features. This was reflected in the 16–17 September comparisons between Q_{RAD} (Figs. 6b,c) and Q_{DP} (Figs. 6e,f), which depicted a significant mitigation of overestimation biases within convective features while recording a steady or slightly increased underestimation biases in stratiform regions. The mean bias ratio for QDP for 16–17 September were decreased to 0.760 and 0.718, respectively.

b. Gauge-corrected radar daily accumulations

Application of the local gauge-correction scheme tempered the various biases in the Q_{DP} scheme for both Harvey (Figs. 5g–i) and Florence (Figs. 6g–i). Most bias ratios comparisons for individual CoCoRaHS gauges were either within the normal bias range (0.90–1.10) or classified with a notable underestimation bias (<0.90). The 3-day average mean bias ratio for Harvey decreased to 0.869 (Table 3). This signified that the inclusion of a local gauge correction scheme created a greater underestimation bias when compared to Q_{DP}. The significant precipitation underestimation biases related to the various radar outages during Florence were partially mitigated with the MRMS local gauge-correction scheme, but still resulted in an overall underestimation ratio value of 0.893 (Table 4). Despite the resultant underestimation bias, the MAE for both storms were reduced by 13.7% and 34.0%, respectively, and the correlation coefficient values were improved, especially a 0.045 increase in the 3-day average to 0.941 for Florence.

The Q_{WC} product using the wind-corrected gauges resulted in increased precipitation totals across both domains. Daily bubble plots for Hurricanes Harvey (Figs. 5j–l) and Florence
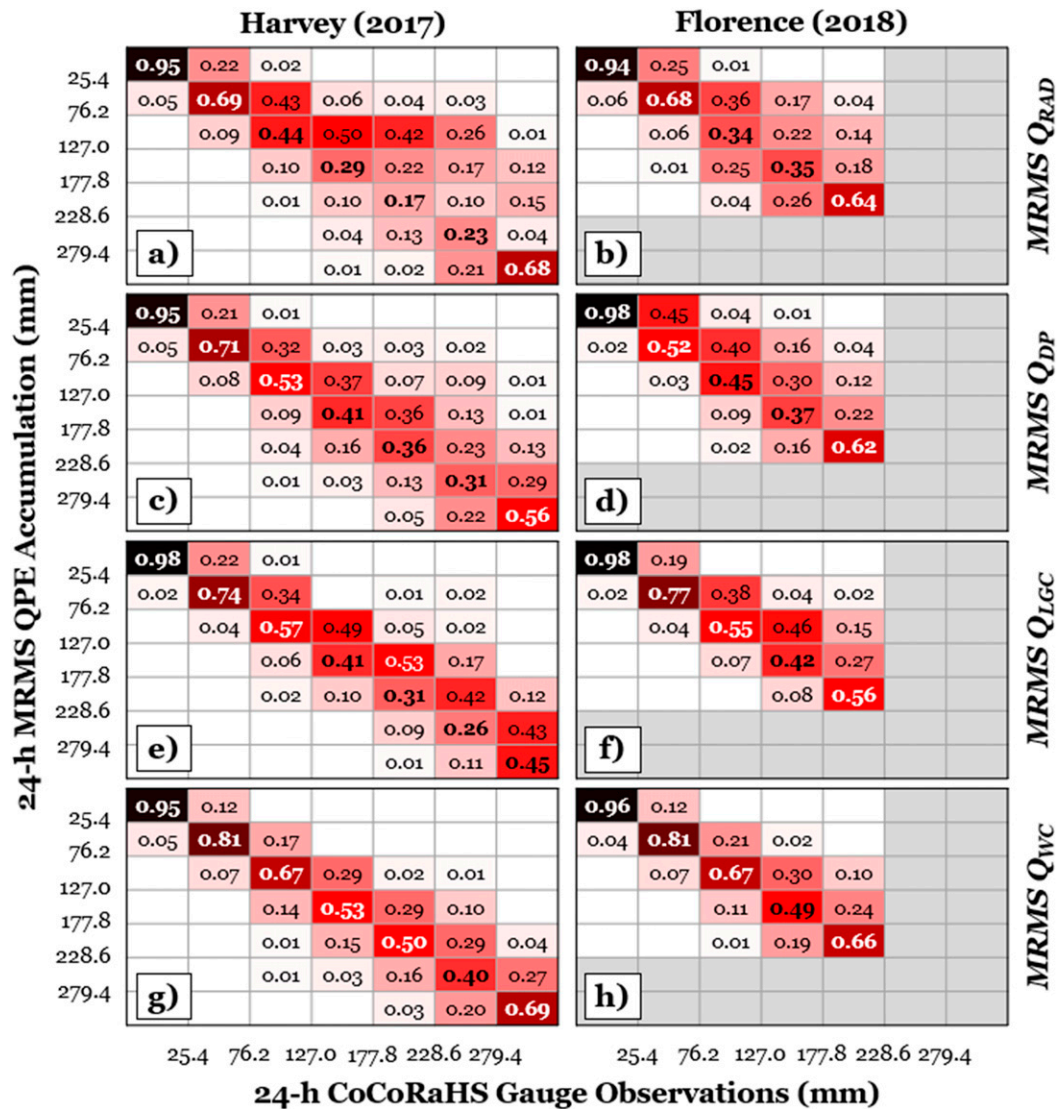
FIG. 8. Error matrices of 24-h QPE accumulations vs CoCoRaHS gauge observations for (left) Hurricane Harvey and (right) Hurricane Florence for the following MRMS products: (a),(b) Q_{RAD}; (c),(d) Q_{DP}; (e),(f) Q_{LGC}; and (g),(h) Q_{WC}. The 24-h accumulations are binned into ranges for values of <25.4 mm (1.00 in.), >279.4 mm (11.00 in.), and 50.8-mm intervals between 25.4 and 279.4 mm. There were insufficient sample sizes for bins exceeding 228.6 mm (9.00 in.) for Hurricane Florence. Darker shades of red represent a greater ratio of values that fall into the respective bin. Matrix grid cells containing bold numbers represent the ideal range that MRMS QPE vs CoCoRaHS gauge pairs should fall into.

(Figs. 6j–l) depicted more gauge comparisons within an ideal bias ratio range of 0.90–1.10 when compared to the Q_{LGC} bubble plots. The 3-day average mean bias ratio increased to 0.986 for Harvey during the period 26–28 August 2017 (Table 3) and 0.984 for Florence during the period 15–17 September 2018 (Table 4). This signified that the underestimation bias created within the Q_{LGC} product was removed in Q_{WC}. The average MAE values were reduced by 8.5% for Harvey and 6.0% for Florence, yet the correlation coefficient values had minimal changes.

Comparisons of daily accumulations of the MRMS QPE products for the duration of each tropical cyclone characterized

the improvement of skill from the radar-based approaches to the final conceptual Q_{WC} product. The two MRMS radar-only schemes struggled with the accuracy of precipitation totals > 76.2 mm; moreover, distinct underestimation biases were characterized throughout the various accumulation ranges (Figs. 8a–d). The Q_{LGC} product displayed improvements with daily precipitation totals < 127.0 mm, yet reductions in performance were characterized in the greater accumulation categories (Figs. 8e,f). Applying the wind correction scheme displayed improved error matrices results for all daily precipitation totals > 25.4 mm (Figs. 8g,h) compared to Q_{LGC}; moreover, the greatest percentage of ideal bin
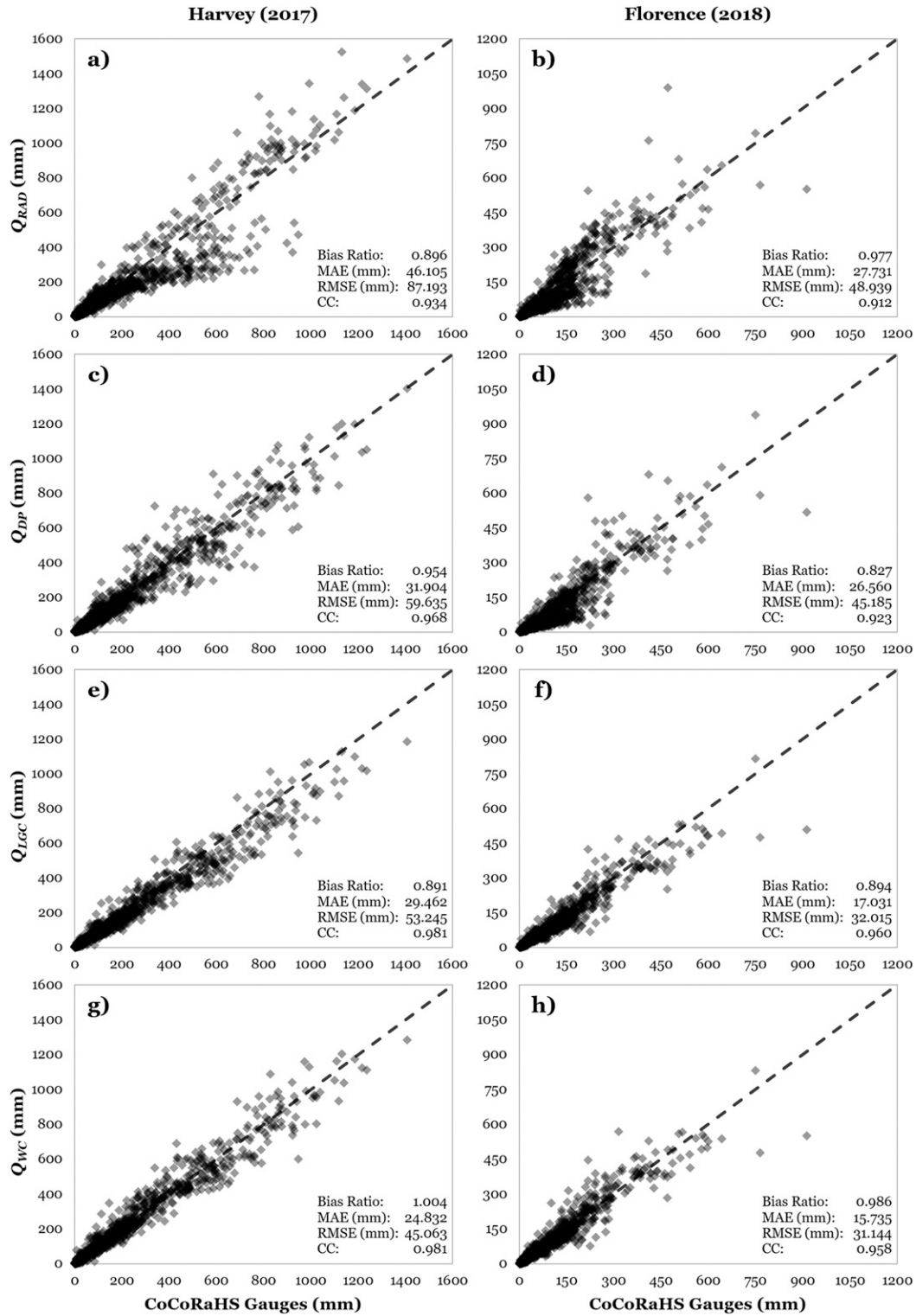
FIG. 9. Scatterplots of storm-total accumulations of (a),(b) Q_{RAD}; (c),(d) Q_{DP}; (e),(f) Q_{LGC}; and (g),(h) Q_{WC} compared to storm-total accumulations of daily CoCoRaHS gauge observations for Hurricanes (left) Harvey and (right) Florence. The dashed line represents the one-to-one line between the CoCoRaHS gauges and the gridded MRMS QPE values. Statistical analyses of each MRMS QPE product are provided in the lower-right corner of each scatterplot.
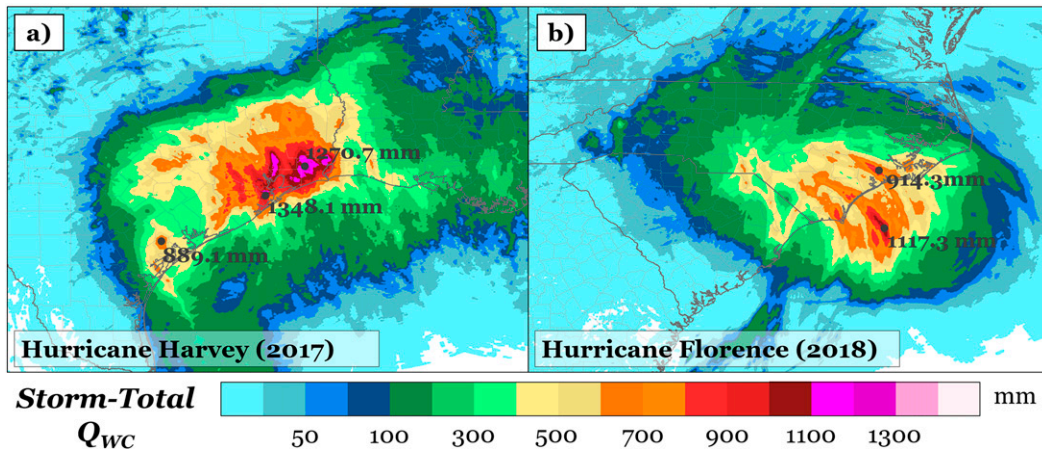
FIG. 10. The storm-total accumulation of Q_{WC} (mm) for (a) Hurricane Harvey from 0000 UTC 24 Aug to 0000 UTC 1 Sep 2017 and (b) Hurricane Florence from 0000 UTC 13 Sep to 0000 UTC 18 Sep 2018. Points on the map denote local precipitation maxima of interest.

matching for all precipitation ranges > 25.4 mm were shown with the Q_{WC} product.

c. Storm-total accumulations

Storm-total accumulations of MRMS QPE products compared to CoCoRaHS gauges demonstrated the improvements going from the different radar-only QPE approaches to the local gauge-correction methodologies. Statistical performances improved from Q_{RAD} to Q_{DP} for both tropical cyclones (Figs. 9a–d). The bimodal data distribution shown for Harvey was mitigated, and the underestimation bias reduced from 0.896 to 0.954. Statistical improvements for Florence were tempered by the multiple radar outages, which also attributed to the bimodal distribution retainment and the underestimation mean bias ratio of 0.827.

The scatterplot spread decreased with Q_{LGC} while improving statistical measures except for the mean bias ratio with Harvey (Figs. 9e,f). The increase in the underestimation bias to 0.891 was attributed to gauge wind undercatch. The mean bias ratio improved for Florence, yet the value of 0.894 was also influenced by gauge wind undercatch. The storm-total mean bias ratio improved to 1.004 for Harvey and to 0.986 for Florence when accounting for wind undercatch errors in Q_{WC} (Figs. 9g,h). Storm-total MAE was improved by 15.7% for Harvey and 7.6% for Florence compared to Q_{LGC}, yet the correlation coefficient was similar between Q_{LGC} and Q_{WC} for both tropical cyclones.

The final storm total Q_{WC} for Hurricane Harvey had three prominent local storm-total maxima in Texas (Fig. 10a). The peak total was 1348.1 mm (53.07 in.) between Santa Fe and Dickinson, Texas, just west of Galveston Bay and south of Houston. This maximum QPE value was located within an elongated region of >1000 mm from Galveston County to Liberty County, which included the eastern portion of the city of Houston. The second prominent local maximum was 1270.7 mm (50.03 in.) near Fannett in Jefferson County, which deviated from the record gauge totals in nearby Nederland (1538.7 mm) and Groves (1537.7 mm) from the

Jefferson County Drainage District (JCDD) rain gauges (Blake and Zelinsky 2018). All other JCDD gauges recorded <1251 mm, and the Q_{WC} product was representative of these observed values. The other notable local precipitation maximum was 889.1 mm (35.00 in.) west of McFadden, Texas, along the path of the center of Harvey.

Storm-total accumulations from Hurricane Florence had broad regions of precipitation totals > 400 mm across southern North Carolina and parts of northeast South Carolina (Fig. 10b). The maximum precipitation estimated by Q_{WC} over land was 914.3 mm (36.00 in.) in an area near Belgrade, North Carolina, within northern Onslow County. This superseded the maximum observed rainfall total of 912.6 mm (35.93 in.) northwest of Elizabethtown in Bladen County and relocated the location of the greatest storm-total accumulation approximately 130 km to the east-northeast. There were three pronounced banding regions of precipitation exceeding 600 mm with localized storm totals > 800 mm. Unverified precipitation estimates off the North Carolina coast exceeded 1100 mm.

The wind corrected gauge observations and its interpolation of adjusted observations through the locally gauge-correcting QPEs process resulted in notable storm-total accumulation differences between Q_{LGC} and Q_{WC}. Most regions impacted by Harvey had the storm-total precipitation increased by 50–75 mm with some localized rainfall adjustments > 75 mm (Fig. 11a). The most pronounced adjustment was near the region of landfall with an upward adjustment of 100–225 mm due to greater wind magnitudes. Most storm-total precipitation values for Florence increased by 25–50 mm with localized regions having increased >75 mm (Fig. 11b). A broad region along the southern extent of the Outer Banks of North Carolina had the storm-total precipitation increase by >100 mm in Q_{WC}, likely influenced by the slow storm motion and proximity to the center of circulation prior to the southern landfall location.

The comparison of MRMS Q_{WC} to the NWS Stage IV QPE demonstrated how the wind correction of QPE could improve storm total values (Fig. 12). Regions beyond areas of prolonged
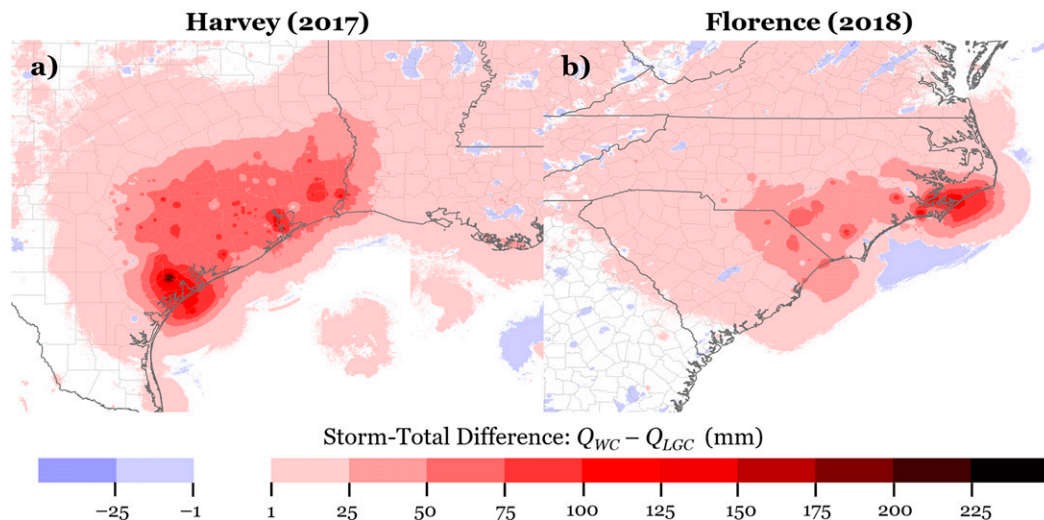
FIG. 11. Storm-total accumulation difference between Q_{WC} and Q_{LGC} (mm) for (a) Hurricane Harvey from 0000 UTC 24 Aug to 0000 UTC 1 Sep 2017 and (b) Hurricane Florence from 0000 UTC 13 Sep to 0000 UTC 18 Sep 2018.

convective influence saw improvements of 50–150 mm over Stage IV. MRMS Q_{WC} values near the area of landfall with Harvey had accumulations 100–300 mm greater than Stage IV (Fig. 14e). Similar influences can be seen near the area of landfall for Florence away from the greater values resulting from convective features (Fig. 14f). Variations in the Q_{WC} product versus Stage IV, including where Q_{WC} values were lower than Stage IV in regions defined by prolonged residing of convective bands, can be attributed to the use of different radar-derived QPE products for Stage IV generation, different gauge networks for bias corrections, and the use of CoCoRaHS gauges in the Stage IV product, yet the influence of correcting for wind undercatch through Q_{WC} can be beneficial to the Stage IV values.

5. Discussion of wind correction for QPE generation

a. Influence and uncertainty of Q_{WC}

The implementation of a single conceptual wind correction scheme across numerous gauge networks demonstrated how it can improve the quality of QPE values. The findings between Q_{LGC} and Q_{WC} reinforced the importance of mitigating the uncertainty of gauge observations from wind turbulence; moreover, the application of a wind correction technique significantly altered precipitation values during these tropical cyclones.

Influence of the prototyped wind correction scheme can be demonstrated through hourly analysis at gauge sites during Harvey. AFWT2 near San Antonio Bay, Texas recorded 416.1 mm over a 48-h period ending 0000 UTC 27 August, whereas applying the conceptual wind correction technique adjusted the 48-h total to 560.3 mm (Fig. 13a). The period from 0300 to 0900 UTC 26 August was characterized by a >8 mm increase per hour (i.e., an upward adjustment of 34%–59% h^{-1}) based on estimated winds of 10.0–16.1 m s^{-1} near the

approximated gauge orifice height. MFNT2 near McFaddin, Texas, experienced more convective rainfall associated with the eyewall structure, which led to greater rainfall accumulation adjustments (Fig. 13b). The hourly accumulations ending at 0700 UTC and 1100–1300 UTC 26 August depicted >19 mm correction of the gauge observation per hour, most notably at 1200 UTC when the value at MFNT2 increased from 82.0 to 109.4 mm based on a HRRR 10 m AGL wind value adjusted to a 1 m AGL wind of 9.8 m s^{-1}. The 48-h total at MFNT2 for the period ending 1200 UTC 27 August increased from 627.6 to 831.8 mm.

Numerous assumptions were made to accommodate the proposed wind correction scheme across various networks. Metadata associated with gauge networks usually consist of only the latitude and longitude coordinates. The authors assert that the broad assumptions about the characteristics of each gauge are insufficient toward the application of any gauge correction technique within a system like MRMS that ingests numerous gauge networks of differing qualities and instrumentation characteristics. The development of a more advanced system to account for the wind undercatch of gauges would require additional metadata than what is currently available, including characteristics such as gauge type (i.e., tipping bucket, weighing, etc.), the diameter of the gauge orifice, and the presence of a windshield and its configuration.

Another limitation of the scheme was the application of the HRRR 10 m AGL wind and its interpolation as the near-surface wind field. It was considered to be representative of the near-surface conditions for the events in this study, yet one must recognize and understand the potential biases of NWP systems (e.g., Fovell and Gallagher 2020). The use of observed winds would be more practical, yet not all rain gauge sites have an anemometer. Accurate 10 m AGL model wind fields or observed anemometer wind speeds should be interpolated down to the height of the gauge opening if not measured at the
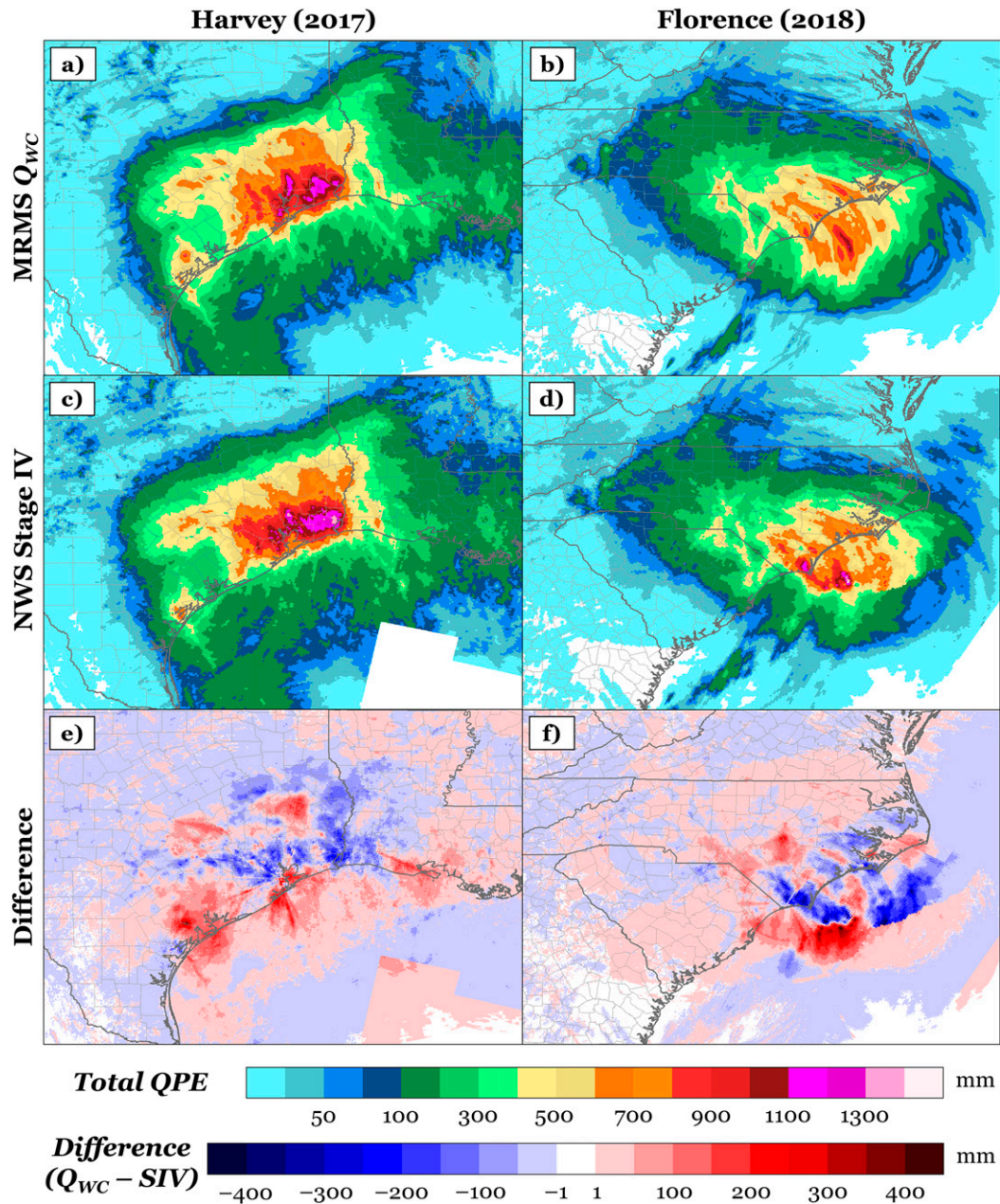
FIG. 12. Accumulation of (a),(b) MRMS Q_{WC}; (c),(d) NWS Stage IV QPE; and (e),(f) the difference between the two (Q_{WC} minus NWS Stage IV QPE) for (left) Hurricane Harvey and (right) Hurricane Florence. Comparisons for Harvey were conducted from 1200 UTC 24 Aug to 1200 UTC 31 Aug 2017. Comparisons for Florence were conducted from 1200 UTC 13 Sep to 1200 UTC 17 Sep 2018.

gauge level. This would require having the height of the gauge and associated anemometer, if one is present, with an expanded gauge metadata set. The HRRR 10 m AGL wind magnitude was utilized as a single value representing the entire hour, yet variations in wind magnitude throughout a given hour regardless of source (model or observed) can also influence the corrected gauge observation (e.g., Duchon and Essenberg 2001).

Studies investigating the impact and correction of gauge wind undercatch during rainfall events were based on wind speeds only up to 7–15 m s^{-1} at different time scales; thus, available equations were extrapolated within the prototype framework to be applied at the hourly scale for tropical cyclones where wind speeds commonly exceed 20 m s^{-1}. Drop size distributions in tropical cyclones were observed to be smaller and in greater concentration compared to convective
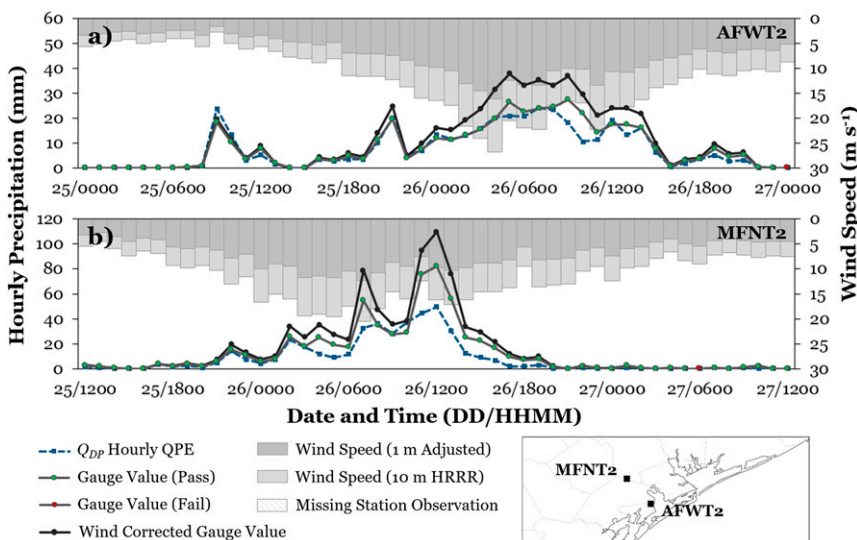
FIG. 13. Time series of various hourly precipitations for the gauges (a) AFWT2 and (b) MFNT2 for various 48-h periods during Hurricane Harvey. Included in the time series are Q_{DP} hourly accumulations (blue dashed line), observed hourly gauge accumulations (solid gray line) with points representing if the gauge passed (green) or failed (red) the MRMS gauge QC algorithm, the wind corrected gauge value (solid black line), the 1 m AGL adjusted wind speed used in the wind correction calculation (light gray bars), and the HRRR 10 m AGL wind speed which the 1-m adjusted winds were derived from (gray bars). Hours with missing gauge observations have the respective columns filled with a light gray hatching. The map in the lower-right corner shows the location of each gauge.

storms (e.g., Tokay et al. 2008; Chang et al. 2009). Smaller drop masses would be more susceptible to wind turbulence; thus, it is plausible that current wind correction equations might not be representative in greater wind velocities and that certain gauge characteristics (e.g., windshields) could have a more significant impact on modifying gauge measurements.

Verification of the wind correction scheme was conducted under the assumption that CoCoRaHS gauge observations were accurate, yet it was noted that they can still be influenced by wind undercatch despite a smaller orifice (e.g., Nešpor and Sevruk 1999). It is unknown what that wind corrective factor for CoCoRaHS-style gauges would be. While the comparisons between CoCoRaHS observations and Q_{WC} in this study resulted in near-ideal bias ratio values, the authors assert that the unknown wind impacts on the independent CoCoRaHS observations could suggest that Q_{WC} could still be underestimating precipitation amounts, thus creating greater uncertainty beyond the other aforementioned challenges.

b. Observational density influence

Another by-product of the wind correction scheme was the localized influences of enhanced gauge observation values in the local gauge-correction scheme, especially in areas with sparse gauge densities. Difference fields between Q_{LGC} and Q_{WC} for both tropical cyclones depicted this challenge (Fig. 11). The local storm-total accumulation maximum west of McFadden, Texas from MFNT2 highlights significant regional adjustments of QPE values from a single observation point (Fig. 10a). The continuous reporting of

only a single gauge over a substantial area resulted in a localized maximum exhibiting an increase of >125 mm resulting in storm-total QPEs > 600 mm; thus, it is likely that the storm-total precipitation in the landfall region beyond the localized influence from MFNT2 was underrepresented.

Most gauge observations surrounding MFNT2 were likely damaged or failed to transmit during the landfall of Harvey. The IDW scheme employed for Q_{LGC} and Q_{WC} works well in areas of ample gauge coverage; however, reduced gauge densities along with significant differences between the gauge and gridded radar QPE would lend itself to having the local influence of the gauge stand out. The number of reporting hourly gauge observations decreased by 21% during Harvey and 12% during Florence over a 72-h period across the entire domain (Fig. 14). Available gauge observations prior to and after landfall near the landfall location were substantially decreased, especially where estimated winds were >50 kt (25.7 m s^{-1}). The limited domains selected for both tropical cyclones in Fig. 14 contained a more than 40% decrease in gauges that reported every hour, while the number of gauges that went completely missing post-landfall increased by 77 sites for Harvey and 62 sites for Florence.

The percent of observations that failed QC per hour more than doubled during the same 72-h period (Fig. 15). Less than 10% of hourly gauge accumulations failed the MRMS gauge QC algorithm prior to the landfall of Harvey. The post-landfall gauge failure rate peaked at 26.1% on 1600 UTC 27 August. The observational failure rate during Florence increased from 11.6% at the beginning of the period to a peak failure rate of
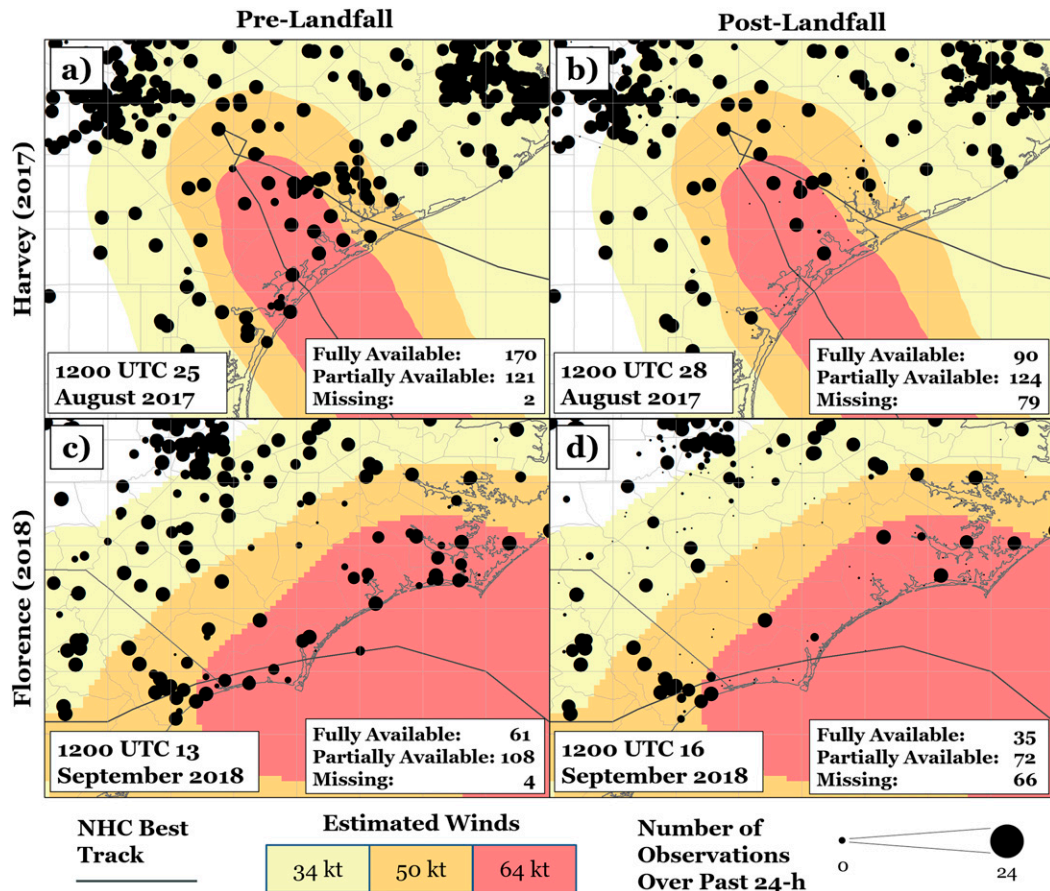
FIG. 14. Depiction of available gauge observations for (a),(b) Hurricane Harvey and (c),(d) Hurricane Florence for a 24-h period (left) pre-landfall and (right) post-landfall. Each gauge within the respective domains were sized based on the number of observations available that hour regardless of passing or failing the MRMS QC algorithm. The smallest gauge points represent no available observations during the past 24 h, and the largest gauge points represent all observations were available. Also plotted are the best track and the estimated wind speeds of 34, 50, and 64 kt ($1\,kt \approx 0.51\,m\,s^{-1}$) for each tropical cyclone as provided by the National Hurricane Center (NHC; https://www.nhc.noaa.gov).

31.8% at 1800 UTC 16 September. Reasons for increased failed observations included significant differences between the gauge versus Q_{DP} due to radar overshooting key precipitation features and adverse impacts to the gauge (e.g., damage to the instrument) but continued to transmit the observation. Having an increased failure rate of gauge observations combined with the increased number of sites not reporting further exacerbated the challenge of obtaining quality gauge accumulations needed for widespread adjustments of radar-derived QPE.

6. Summary

The various radar and gauge-based products within the MRMS system allowed for a comprehensive analysis of two historic tropical cyclone rainfall events: Hurricane Harvey (2017) and Hurricane Florence (2018). The traditional reflectivity-based rain rate scheme created a bimodal distribution of precipitation totals. The efficient tropical stratiform-based precipitation

was generally underestimated, while the convective-based features were shown to have notable QPE overestimations. Implementation of a synthetic dual-polarization scheme within the MRMS framework showed mitigation of the various QPE biases where radars were operational, yet there remained uncertainty in the accuracy of the radar-derived QPEs given the scatter of data.

Local gauge correction of the Q_{DP} product showed overall improvements in the storm-total accumulation when compared to independent CoCoRaHS gauge observations; however, the Q_{LGC} product had a consistent underestimation bias for both tropical cyclones, which in some cases was worse than the two radar-only products. Wind undercatch during these tropical cyclones influenced the hourly gauge observations and degraded the MRMS Q_{LGC} product accuracy. A conceptual wind-correction scheme was introduced to reduce wind-induced underestimation biases. The prototype wind-correction scheme was designed from past wind undercatch studies and designed to be generically applied to gauges
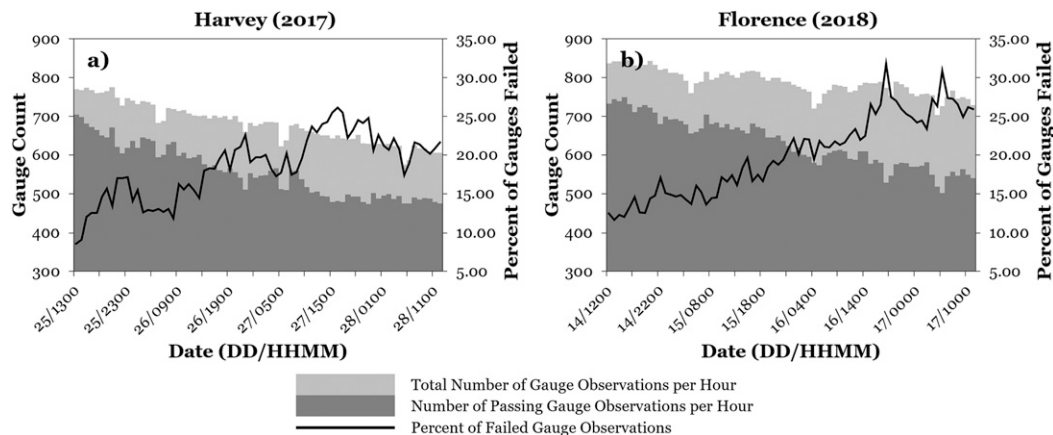
FIG. 15. Total number of hourly gauge observations available (light gray) and number of passing observations (dark gray) along with the percent of gauge observations that failed (solid black line) during (a) Hurricane Harvey for the hourly observations ending 1300 UTC 25 Aug–1200 UTC 28 Aug 2017 and (b) Hurricane Florence for the hourly observations ending 1200 UTC 14 Sep–1100 UTC 17 Sep 2018.

regardless of the instrumentation characteristics. The application of the wind correction scheme demonstrated a notable improvement in the storm-total mean bias ratio in the developed Q_{WC} product. Analysis of individual gauge sites depicted significant adjustments of the hourly gauge observations, including instances of increasing the hourly accumulations at some gauge sites by >30% h^{-1}.

Various challenges and limitations were identified in the application of the wind undercatch correction scheme. The lack of gauge characteristic metadata resulted in a number of simplifications and assumptions in the scheme; moreover, past studies that derived equations focused on wind speeds up to 15 m s^{-1}, which is below the threshold for tropical storm classification, and past studies did not explicitly analyze events characterized by tropical warm rain processes, which produce smaller drop size distributions more prone to wind undercatch.

Other challenges exist with generating accurate precipitation amounts from tropical cyclones. Analysis of the two MRMS radar-derived QPE highlighted the uncertainty in using different radar variables to estimate precipitation in tropical cyclones. Techniques such as probabilistic QPE (Kirstetter et al. 2015) can potentially quantify the uncertainty in radar-derived QPEs. Additional radar-based limitations include data sampled at farther distances that may overshoot critical warm-rain processes and unrepresentative rain-rate relationships to employ with efficient tropical rainfall; thus, it is critical to have accurate surface observations to verify and correct any biases in radar-derived QPEs. While adjusted gauge observations can improve the accuracy of gridded QPEs through bias correction schemes, the local influence of the gauge could be minimized if there are a lack of observations.

The uncertainty and assumptions depicted in this study characterize the challenges of obtaining precise precipitation estimates in conditions defined by strong winds. Future studies on the behavior and correction of gauge observations during tropical cyclones combined with the extensive metadata necessary to apply wind undercatch corrections could advance the

understanding of how much rainfall truly accumulates in these prolific tropical cyclone rainfall events. The need to apply wind correction strategies beyond gauge observations, especially when observations are lacking, is also an area of research that would require further exploration.

REFERENCES

Allerup, P., and H. Madsen, 1980: Accuracy of point precipitation measurements. *Nord. Hydrol.*, **11**, 57–70, https://doi.org/10.2166/nh.1980.0005.

Benjamin, S. G., and Coauthors, 2016: A North American hourly assimilation and model forecast cycle: The Rapid Refresh. *Mon. Wea. Rev.*, **144**, 1669–1694, https://doi.org/10.1175/MWR-D-15-0242.1.

Blake, E. S., and D. A. Zelinsky, 2018: Hurricane Harvey. NOAA/National Hurricane Center Tropical Cyclone Rep., 77 pp., https://www.nhc.noaa.gov/data/tcr/AL092017_Harvey.pdf.

Chang, W., T. C. Wang, and P. Lin, 2009: Characteristics of the raindrop size distribution and drop shape relation in typhoon systems in the western Pacific from the 2D video disdrometer and NCU C-band polarimetric radar. *J. Atmos. Oceanic Technol.*, **26**, 1973–1993, https://doi.org/10.1175/2009JTECHA1236.1.

Cifelli, R., N. Doesken, P. Kennedy, L. D. Carey, S. A. Rutledge, C. Gimmestad, and T. Depue, 2005: The Community Collaborative Rain, Hail, and Snow network: Informal education for scientists and citizens. *Bull. Amer. Meteor. Soc.*, **86**, 1069–1078, https://doi.org/10.1175/BAMS-86-8-1069.

Cocks, S. B., S. M. Martinaitis, B. Kaney, J. Zhang, and K. Howard, 2016: MRMS QPE performance during the 2013/14 cool season. *J. Hydrometeor.*, **17**, 791–810, https://doi.org/10.1175/JHM-D-15-0095.1.

——, J. Zhang, S. M. Martinaitis, Y. Qi, B. Kaney, and K. Howard, 2017: MRMS QPE performance east of the Rockies during the 2014 warm season. *J. Hydrometeor.*, **18**, 761–775, https://doi.org/10.1175/JHM-D-16-0179.1.

——, and Coauthors, 2019: A prototype quantitative precipitation estimation algorithm for operational S-band polarimetric radar utilizing specific attenuation and specific differential phase. Part II: Performance verification and case study analysis. *J. Hydrometeor.*, **20**, 999–1014, https://doi.org/10.1175/JHM-D-18-0070.1.

Daly, C., W. P. Gibson, G. H. Taylor, M. K. Doggett, and J. I. Smith, 2007: Observer bias in daily precipitation measurements at United States cooperative network stations. *Bull. Amer. Meteor. Soc.*, **88**, 899–912, https://doi.org/10.1175/BAMS-88-6-899.

Duchon, C. E., and G. R. Essenberg, 2001: Comparative rainfall observations from pit and aboveground rain gauges with and without wind shields. *Water Resour. Res.*, **37**, 3253–3263, https://doi.org/10.1029/2001WR000541.

Førland, E. J., and I. Hanssen-Bauer, 2000: Increased precipitation in the Norwegian Arctic: True or false? *Climatic Change*, **46**, 485–509, https://doi.org/10.1023/A:1005613304674.

——, and Coauthors, 1996. Manual for operational correction of Nordic precipitation data. Norwegian Meteorological Institute Rep. 24/96, 66 pp.

Fovell, R. G., and A. Gallagher, 2020: Boundary layer and surface verification of the High-Resolution Rapid Refresh, version 3. *Wea. Forecasting*, **35**, 2255–2278, https://doi.org/10.1175/WAF-D-20-0101.1.

Helms, D., P. Miller, M. Barth, D. Starosta, B. Gordon, S. Schofield, F. Kelly, and S. Koch, 2009: Status update of the transition from research to operations of the Meteorological Assimilation Data Ingest System. *25th Conf. on Int. Interactive Information and Processing Systems*, Phoenix, AZ, Amer. Meteor. Soc., 5A.3, https://ams.confex.com/ams/89annual/techprogram/paper_149883.htm.

Kim, D., B. Nelson, and D. J. Seo, 2009: Characteristics of reprocessed Hydrometeorological Automated Data System (HADS) hourly precipitation data. *Wea. Forecasting*, **24**, 1287–1296, https://doi.org/10.1175/2009WAF2222227.1.

Kirstetter, P.-E., J. J. Gourley, Y. Hong, J. Zhang, S. Moazamigoodarzi, C. Langston, and A. Arthur, 2015: Probabilistic precipitation rate estimates with ground-based radar networks. *Water Resour. Res.*, **51**, 1422–1442, https://doi.org/10.1002/2014WR015672.

Lin, Y., and K. E. Mitchell, 2005: The NCEP stage II/IV hourly precipitation analyses: Development and applications. *19th Conf. on Hydrology*, San Diego, CA, Amer. Meteor. Soc., 1.2, http://ams.confex.com/ams/pdfpapers/83847.pdf.

Martinaitis, S. M., H. M. Grams, C. Langston, J. Zhang, and K. Howard, 2018: A real-time evaporation correction scheme for radar-derived mosaicked precipitation estimations. *J. Hydrometeor.*, **19**, 87–111, https://doi.org/10.1175/JHM-D-17-0093.1.

Medlin, J. M., S. K. Kimball, and K. G. Blackwell, 2007: Radar and rain gauge analysis of the extreme rainfall during Hurricane Danny's (1997) landfall. *Mon. Wea. Rev.*, **135**, 1869–1888, https://doi.org/10.1175/MWR3368.1.

Nešpor, V., and B. Sevruk, 1999: Estimation of wind-induced error of rainfall gauge measurements using a numerical simulation. *J. Atmos. Oceanic Technol.*, **16**, 450–464, https://doi.org/10.1175/1520-0426(1999)016<0450:EOWIEO>2.0.CO;2.

Qi, Y., and J. Zhang, 2017: A physically based two-dimensional seamless reflectivity mosaic for radar QPE in the MRMS system. *J. Hydrometeor.*, **18**, 1327–1340, https://doi.org/10.1175/JHM-D-16-0197.1.

——, ——, P. Zhang, and Q. Cao, 2013: VPR correction of bright band effects in radar QPEs using polarimetric radar observations. *J. Geophys. Res. Atmos.*, **118**, 3627–3633, https://doi.org/10.1002/jgrd.50364.

——, S. Martinaitis, J. Zhang, and S. Cocks, 2016: A real-time automated quality control of hourly rain gauge data based on multiple sensors in MRMS system. *J. Hydrometeor.*, **17**, 1675–1691, https://doi.org/10.1175/JHM-D-15-0188.1.

Ryzhkov, A., M. Diederich, P. Zhang, and C. Simmer, 2014: Potential utilization of specific attenuation for rainfall estimation, mitigation of partial beam blockage, and radar networking. *J. Atmos. Oceanic Technol.*, **31**, 599–619, https://doi.org/10.1175/JTECH-D-13-00038.1.

Stewart, S. R., and R. Berg, 2019: Hurricane Florence. NOAA/National Hurricane Center Tropical Cyclone Rep., 98 pp. https://www.nhc.noaa.gov/data/tcr/AL062018_Florence.pdf.

Tang, L., J. Zhang, C. Langston, J. Krause, K. Howard, and V. Lakshmanan, 2014: A physically based precipitation–nonprecipitation radar echo classifier using polarimetric and environmental data in a real-time national system. *Wea. Forecasting*, **29**, 1106–1119, https://doi.org/10.1175/WAF-D-13-00072.1.

Tokay, A., P. G. Bashor, E. Habib, and T. Kasparis, 2008: Raindrop size distribution measurements in tropical cyclones. *Mon. Wea. Rev.*, **136**, 1669–1685, https://doi.org/10.1175/2007MWR2122.1.

Wang, Y., S. Cocks, L. Tang, A. Ryzhkov, P. Zhang, J. Zhang, and K. Howard, 2019: A prototype quantitative precipitation estimation algorithm for operational S-band polarimetric radar utilizing specific attenuation and specific differential phase: Part I-Algorithm description. *J. Hydrometeor.*, **20**, 985–997, https://doi.org/10.1175/JHM-D-18-0071.1.

Yang, D., B. E. Goodison, J. R. Metcalfe, V. S. Golubev, R. Bataes, T. Pangburn, and C. L. Hanson, 1998: Accuracy of NWS 8″ standard nonrecording precipitation gauge: Results and application of WMO intercomparison. *J. Atmos. Oceanic Technol.*, **15**, 54–68, https://doi.org/10.1175/1520-0426(1998)015<0054:AONSNP>2.0.CO;2.

Zhang, J., and Y. Qi, 2010: A real-time algorithm for the correction of brightband effects in radar-derived QPE. *J. Hydrometeor.*, **11**, 1157–1171, https://doi.org/10.1175/2010JHM1201.1.

——, ——, K. Howard, C. Langston, and B. Kaney, 2012: Radar Quality Index (RQI) – A combined measure of beam blockage and VPR effects in a national network. *IAHS Publ.*, **351**, 388–393.

——, and Coauthors, 2016: Multi-Radar Multi-Sensor (MRMS) quantitative precipitation estimation: Initial operating capabilities. *Bull. Amer. Meteor. Soc.*, **97**, 621–638, https://doi.org/10.1175/BAMS-D-14-00174.1.

——, L. Tang, S. Cocks, P. Zhang, A. Ryzhkov, K. Howard, C. Langston, and B. Kaney, 2020: A dual-polarization radar synthetic QPE for operations. *J. Hydrometeor.*, **21**, 2507–2521. https://doi.org/10.1175/JHM-D-19-0194.1.